Title

High-entropy halide perovskite single crystals stabilized by mild chemistry

Journal

Nature, 621(7978)

ISSN

0028-0836

Authors

Folgueras, Maria C
Jiang, Yuxin
Jin, Jianbo
et al.

Publication Date

2023-09-14

DOI

10.1038/s41586-023-06396-8

Peer reviewed

High entropy halide perovskite single crystals stabilized by mild chemistry

Maria C. Folgueras,[1,3,4,#] Yuxin Jiang,[2,3,#] Jianbo Jin,[2] and Peidong Yang[1,2,3,4,*]

[1]Department of Materials Science and Engineering, University of California, Berkeley, Berkeley, California 94720, United States.

[2]Department of Chemistry, University of California, Berkeley, Berkeley, California 94720, United States.

[3]Materials Sciences Division, Lawrence Berkeley National Laboratory, Berkeley, California 94720, United States.

[4]Kavli Energy NanoScience Institute, Berkeley, California 94720, United States.

[#]These authors contributed equally.

*Corresponding author. Email: p_yang@berkeley.edu

Abstract

High entropy materials are excellent candidates for a range of functional materials but traditionally require high-temperature synthetic procedures over 1000°C and complex processing techniques such as hot rolling to form[1–5]. One route to address the extreme synthetic requirements for high entropy materials should involve designing crystal structures with ionic bonding networks and low cohesive energies. Here, we develop room-temperature (20°C) and low-temperature (80°C) solution synthesis procedures for a new class of metal-halide perovskite high entropy semiconductor (HES) single crystals. Due to the soft, ionic lattice nature of the class of metal-halide perovskites, these HES single crystals are designed on the cubic Cs_2MCl_6 ($M = Zr^{4+}$, Sn^{4+}, Te^{4+}, Hf^{4+}, Re^{4+}, Os^{4+}, Ir^{4+}, or Pt^{4+}) vacancy-ordered double perovskite structure from the self-assembly of stabilized complexes in multielement inks, namely free Cs^+ cations and 5 or 6 different isolated $[MCl_6]^{2-}$ anionic octahedral molecules well-mixed in strong hydrochloric acid. The resulting single-phase single crystals span two HES families of 5- and 6-elements occupying the M-site as a random alloy in near-equimolar ratios, with the overall Cs_2MCl_6 crystal structure and stoichiometry maintained. The incorporation of various $[MCl_6]^{2-}$ octahedral molecular orbitals disordered across the high entropy 5- and 6-element Cs_2MCl_6 single crystals produces complex vibrational and electronic structures with energy transfer interactions between the confined exciton states of the 5 or 6 different isolated octahedral molecules.

Main text

High entropy alloys (HEAs) have been increasingly studied across a range of material classes, particularly high entropy metals (HEMs) and high entropy ceramics (HECs), for their exceptional functional properties[1–5], leaving much to be explored in the field of high entropy semiconductors (HESs)[6–8]. However, across all reported HEM, HEC, and HES spaces, a significant disadvantage to their synthetic procedure is the extreme temperature requirements necessary to form single-phase, crystalline solid solutions (typically >1000°C)[9–12], temperatures which can often be incompatible with the stability of other materials in a device architecture[13]. Therefore, a critical component in the discovery of novel HES material systems should include

the design of synthetic procedures utilizing significantly milder conditions. Due to their soft, easily reconfigurable lattices[14,15] and facile, low-to-mild-temperature solution processability[16,17], halide-based perovskites offer a potential solution to this design challenge. In this work, we explore the vacancy-ordered double perovskite Cs_2MCl_6 crystal structure[18] as a platform for creating high entropy halide perovskite semiconductor single crystals within the $Cs_2\{ZrSnTeHfRePt\}_1Cl_6$ and $Cs_2\{SnTeReOsIrPt\}_1Cl_6$ HES families using room-temperature (20°C) and low-temperature (80°C) solution syntheses, respectively. These single-phase systems contain near-equimolar ratios of disordered 5 and 6 different $[M^{4+}Cl_6]^{2-}$ octahedra within each single crystal domain. Confined exciton states form for each $[MCl_6]^{2-}$ octahedral complex within the bulk HES crystal[19,20], generating a probability for fast excitonic relaxation to the more strongly confined exciton states via energy transfer[21,22].

Building on our previous work of octahedral ink formation from Cs_2TeX_6 ($X = Cl^-$, Br^-, I^-) powders[17], the appropriate 1-element Cs_2ZrCl_6, Cs_2SnCl_6, Cs_2TeCl_6, Cs_2HfCl_6, Cs_2ReCl_6, Cs_2OsCl_6, Cs_2IrCl_6, and Cs_2PtCl_6 starting powders (Supplementary Section 1, Supplementary Figs. 1 and 2, Supplementary Tables 1–4) are dissolved into a single, well-mixed 12 M hydrochloric acid (HCl) solution to generate multielement inks of free Cs^+ cations and isolated $[MCl_6]^{2-}$ ($M = Zr^{4+}$, Sn^{4+}, Te^{4+}, Hf^{4+}, Re^{4+}, Os^{4+}, Ir^{4+}, or Pt^{4+}) anionic octahedral molecules (Fig. 1a). A (re)crystallization process from these multielement inks (Fig. 1a) is used to achieve single crystals within the $Cs_2\{SnTeReOsIrPt\}_1Cl_6$ (i.e., STROIP) and $Cs_2\{ZrSnTeHfRePt\}_1Cl_6$ (i.e., ZSTHRP) HES families. The STROIP HES family spans low entropy[23] 2-element $Cs_2\{SnTe\}_1Cl_6$ (i.e., SnTe), medium entropy[23–25] 3-element $Cs_2\{SnTePt\}_1Cl_6$ (i.e., SnTePt) and 4-element $Cs_2\{SnTeIrPt\}_1Cl_6$ (i.e., SnTeIrPt), and high entropy 5-element $Cs_2\{SnTeReIrPt\}_1Cl_6$ (i.e., SnTeReIrPt) and 6-element $Cs_2\{SnTeReOsIrPt\}_1Cl_6$ (i.e., SnTeReOsIrPt) single crystals. The ZSTHRP HES family spans low entropy 2-element $Cs_2\{ZrHf\}_1Cl_6$ (i.e., ZrHf), medium entropy 3-element $Cs_2\{ZrTeHf\}_1Cl_6$ (i.e., ZrTeHf) and 4-element $Cs_2\{ZrSnTeHf\}_1Cl_6$ (i.e., ZrSnTeHf), and high entropy 5-element $Cs_2\{ZrSnTeHfPt\}_1Cl_6$ (i.e., ZrSnTeHfPt) and 6-element $Cs_2\{ZrSnTeHfRePt\}_1Cl_6$ (i.e., ZrSnTeHfRePt) single crystals. The solution syntheses developed to produce these HES single crystals are the first known syntheses to create any high entropy material (across HEMs, HECs, and other HESs) utilizing room-temperature (20°C) or low-temperature (80°C) procedures. Furthermore, any combination of proposed M-site metal centers

can be utilized to synthesize HES single crystals, thus generating a library of 2-, 3-, 4-, 5-, and 6-element single crystals (Supplementary Fig. 3, showing a distinct high entropy 5-element SnTeReOsPt composition).

The resulting high entropy 5-element SnTeReIrPt, 6-element SnTeReOsIrPt, 5-element ZrSnTeHfPt, and 6-element ZrSnTeHfRePt single crystals are on the order of 30–100 μm in size and possess octahedral and cuboctahedral morphologies typical of a face-centered cubic (FCC) crystal structure (Fig. 1b). Powder X-ray diffraction (PXRD) patterns of the 5-element SnTeReIrPt and 6-element SnTeReOsIrPt HES single crystals (Fig. 2a) and of the 5-element ZrSnTeHfPt and 6-element ZrSnTeHfRePt HES single crystals (Fig. 2d) reveal single-phase FCC crystal structures across all 4 compositions. Fine scans over the two prominent FCC reflections (111) and (220) highlight no peak splitting and are well fit with a single Lorentzian function[26,27] as expected for diffraction peaks of a single-phase crystal system (Figs. 2b and 2c for the SnTeReIrPt and SnTeReOsIrPt crystals, Figs. 2e and 2f for the ZrSnTeHfPt and ZrSnTeHfRePt crystals). Furthermore, the lattice parameters of the 4 HES compositions are consistent with those of the constituent 1-element single crystals (Figs. 2a and 2d). Single crystal X-ray diffraction (SCXRD) experiments performed on the 5-element SnTeReIrPt, 6-element SnTeReOsIrPt, 5-element ZrSnTeHfPt, and 6-element ZrSnTeHfRePt single crystals confirm the cubic $Fm\bar{3}m$ space group with lattice parameters of 10.3035 Å, 10.3110 Å, 10.3868 Å, and 10.3742 Å, respectively (Supplementary Tables 5 and 6). Different octahedra types occupy crystallographically equivalent positions in the SCXRD-determined unit cell such that the resulting crystal structure is a FCC lattice of randomly alloyed M-sites (Supplementary Figs. 4 and 5). PXRD and SCXRD studies of all 2-, 3-, and 4-element single crystals (Supplementary Fig. 6 and 7) also reveal phase-pure FCC crystal structures with lattice parameters in line with the constituent 1-element single crystals (Supplementary Tables 7 and 8). To the authors' knowledge, this is the first report of single crystal formation in any HEM, HEC, or HES system.

We turn to extensive elemental analysis to confirm that each of our single-phase FCC crystal systems contain the 5 and 6 different M-site octahedral centers. The energy-dispersive X-ray spectroscopy (EDX) mapping (Fig. 3a) and spectrum (Supplementary Fig. 8) of a high entropy 6-element SnTeReOsIrPt single crystal indicate the incorporation of all 6 elements homogeneously distributed within one single crystal domain. EDX analysis of the high entropy

5-element SnTeReIrPt, 5-element ZrSnTeHfPt, and 6-element ZrSnTeHfRePt single crystals similarly confirm the presence and homogeneous distribution of the expected 5, 5, and 6 M-site elements, respectively (Supplementary Figs. 9–14). The EDX spectra yield an approximate Cs:Cl molar ratio of 2:6 for all 4 HES compositions (Supplementary Table 9), while inductively coupled plasma atomic emission spectroscopy (ICP-AES) is utilized to precisely quantify the molar ratio of the 5 and 6 different M-site metal centers. The high entropy 5-element SnTeReIrPt (Supplementary Fig. 15), 6-element SnTeReOsIrPt (Supplementary Fig. 15), 5-element ZrSnTeHfPt (Fig. 3b), and 6-element ZrSnTeHfRePt single crystals (Fig. 3c) exhibit near-equimolar ratios among the constituent 5 or 6 M-site elements (Supplementary Tables 10–13). Furthermore, the ICP-AES results across all 4 HES compositions indicate an approximate Cs:overall M-site cation (i.e., all 5 or 6 different M-site cations treated as a single M-site cation) molar ratio of 2:1 (Supplementary Table 14). The combined EDX and ICP-AES analyses thus reveal that the stoichiometric values of the Cs cation, overall M-site cation, and the Cl anion in the formula unit are approximately 2, 1, and 6, respectively, with the precise experimentally-determined stoichiometric compositions for the 4 HES crystal systems shown in Supplementary Table 15. As a result, we confirm that all 4 HES crystal structures possess 5 or 6 different M-site octahedral centers in near-equimolar ratios within an overall Cs_2MCl_6 vacancy-ordered double perovskite framework. EDX (Supplementary Figs. 16–21) and ICP-AES analyses (Supplementary Figs. 22 and 23) of all 2-, 3-, and 4-element single crystals elucidate similar compositional results to their high entropy counterparts.

With the establishment of single-phase FCC Cs_2MCl_6 crystal systems containing 5 and 6 different M-site elements in near-equimolar ratios, it becomes critical to have a comprehensive structural understanding of these HES crystals at various length scales, specifically across the atomic/molecular, unit cell, and single domain levels. Raman spectroscopy allows us to explore the local structure of these new multielement crystals. If no vibrational interactions are assumed between the various possible octahedral coordination environments[28] within all crystals across both HES families, it is possible to fingerprint every phonon band to a particular octahedral unit within each single crystal, and the crystal's vibrational structure becomes increasingly more complex with the incorporation of more octahedral molecules (Supplementary Section 2, Supplementary Figs. 24–38). With a greater understanding of the molecular structure from the

Raman analysis, we can reconsider the unit cell level structure. The SCXRD results of the STROIP and ZSTHRP HES families discussed earlier can only determine an average unit cell based solely on electron density. Given that many of the elements incorporated in the HES crystal systems possess similar electron density, most especially the neighboring Re, Os, Ir, and Pt elements, some degree of order could exist in the lattice that is not easily revealed by electron density alone from conventional SCXRD. A related technique that yields more highly resolved electron density, elemental distribution, and potential short-range order information at the unit cell level is multiwavelength anomalous diffraction (MAD)[29]. As a result of the excitation and relaxation processes occurring during these absorption edge-based diffraction experiments, X-ray fluorescence spectra are simultaneously collected across the Re, Os, Ir, and Pt L_3-edges for a 6-element SnTeReOsIrPt single crystal (Supplementary Note, Supplementary Fig. 39). The imaginary component f'' and real component f' of the resulting anomalous scattering factor can then be derived from these X-ray fluorescence spectra[30]. Comparing the Cromer/Liberman theoretically derived f'' and f' and the X-ray fluorescence experimentally derived f'' and f' near the Re, Os, Ir, and Pt L_3-edges in Fig. 4a reveals that the energy values of the expected edges for both components align quite well between theory and experiment. This alignment further confirms the presence of Re, Os, Ir, and Pt within the unit cell of this 6-element SnTeReOsIrPt single crystal.

To visualize the absolute configuration of the 6 different $[MCl_6]^{2-}$ octahedra in this unit cell, we turn to the MAD precession images generated from the *0kl* plane collected near the L_3-edges of Re, Os, Ir, and Pt, all of which show a FCC lattice (Figs. 4b–4e). If any of the four metals are arranged with any local order, then the edges of the diffraction patterns would shift away from the overall FCC lattice. Therefore, the preservation of the FCC lattice that is observed at all edges in all four precession images indicates that all M-site elements in the 6-element SnTeReOsIrPt single crystal are randomly distributed in the unit cell and across the crystal structure (Figs. 4f and 4g). From this more highly resolved structural information, the occupancy of the 4 probed metals on the M-site can be determined due to the relationship between site occupancy and f'' and f' [29]. The occupancy of each metal is close to the expected value of 1 at its characteristic absorption edge (Supplementary Table 16), and these occupancy values allow for the derivation of the M-site metal ratios to ultimately provide complementary elemental

information to the ICP-AES results of the 6-element SnTeReOsIrPt single crystal (Supplementary Table 17). Similar X-ray absorption behavior (Supplementary Figs. 40 and 41) and similar X-ray scattering behavior and overall structural insights (Supplementary Fig. 42, Supplementary Tables 18 and 19) are observed in the MAD analysis of a 6-element ZrSnTeHfRePt single crystal.

The final aspect of a comprehensive structural understanding of the HES compositions involves studying the potential microstructure at the single domain level, which can be readily visualized using backscattered electron (BSE) imaging and electron backscattered diffraction (EBSD). High entropy alloys (HEAs) are traditionally produced as faceted bulk materials with a complex microstructure of significant grain boundaries and varying grain orientations[31]. As a result of this typical behavior in HEA materials (brought about in large part by their preparation procedures), it is crucial to confirm that our faceted HES compositions do not possess a microstructure of either phase-segregated constituent 1-element grains or randomly oriented 5- or 6-element HES grains. The BSE images of a 6-element ZrSnTeHfRePt system (Fig. 5a) reveal uniform phase contrast across all exposed crystal facets, in which phase contrast represents atomic number differences. Uniform atomic number contrast is also found in the BSE images of the complementary 6-element SnTeReOsIrPt system (Supplementary Fig. 43). Therefore, a lack of variation in the atomic number contrast indicates that there is no measurable phase-separation of the 6 different M-site elements into micrograin structures, highlighting that each crystal does not form grains of phase-segregated constituent 1-element compositions. EBSD analysis of a 6-element SnTeReOsIrPt system further confirms the absence of phase-segregated 1-element grains but also confirms the absence of randomly oriented 6-element grains within the single domain. Scanning an approximately $45 \times 50\ \mu m^2$ region across a flat, triangular facet (Fig. 5b) yields an inverse pole figure (IPF) of a single color (Fig. 5c), which corresponds to a single orientation of the FCC (111) close-packed plane (Fig. 5d). Therefore, a lack of IPF orientation variation reveals that the HES crystal is not composed of randomly oriented 6-element HES grains. The EBSD phase map reinforces this conclusion since the scan region possesses a single lattice parameter and thus a single crystal phase (Fig. 5e). Similar results are found from the IPF and phase map of the 6-element ZrSnTeHfRePt system (Supplementary Fig. 44). The combined BSE imaging and EBSD analyses establish that the 5- and 6-element HES systems are indeed

single crystals of disordered constituent $[MCl_6]^{2-}$ octahedra with no microstructure, which strongly corroborates the previous MAD structural evidence.

From the varied structural and spectroscopic evidence presented herein, the STROIP and ZSTHRP HES families represent the first known solution syntheses of high entropy metal-halide perovskite single crystals containing near-equimolar ratios of disordered 5 and 6 different $[MCl_6]^{2-}$ octahedra within a single domain of the cubic Cs_2MCl_6 crystal framework. The multiple disordered octahedral units serve not only as the vibrational centers (Supplementary Section 2) but also as the absorbing and emitting centers in these HES crystals due to the M and Cl orbital character of the highest occupied molecular orbital (HOMO) and the lowest unoccupied molecular orbital (LUMO)[18,32]. As a result of this intrinsic material property, it is very likely that all 5 or 6 different $[MCl_6]^{2-}$ isolated octahedra contribute to the absorption and emission behavior of the 5-element or 6-element HES single crystals, respectively. As hypothesized, the absorption spectra of these HES compositions reflect a superposition of electronic transitions from all 5 or 6 constituent octahedra within the crystal structure. For the 5-element ZrSnTeHfPt single crystals (Fig. 6a, Supplementary Fig. 45), the majority of the absorption spectrum (in the wavelength range of 321–900 nm) has major contributions from the electronic transitions of the $[TeCl_6]^{2-}$ and $[PtCl_6]^{2-}$ octahedral molecules, as observed by the similar absorbance features between this HES composition and the constituent 1-element Cs_2TeCl_6 and Cs_2PtCl_6 single crystals (Supplementary Fig. 45). The $[TeCl_6]^{2-}$ and $[PtCl_6]^{2-}$ octahedral molecules also contribute to the remainder of this absorption spectrum, with the dominant electronic contributions to the wavelength range of 248.5–321 nm originating from the $[ZrCl_6]^{2-}$, $[TeCl_6]^{2-}$, $[HfCl_6]^{2-}$ and $[PtCl_6]^{2-}$ octahedral molecules and with the dominant electronic contributions to the wavelength range of 225–248.5 nm originating from the $[SnCl_6]^{2-}$ and $[PtCl_6]^{2-}$ octahedral molecules. Nearly identical behavior corresponding to the superposition of features from the electronic transitions of all constituent octahedra are observed in the absorption spectra of the 6-element ZrSnTeHfRePt, 5-element SnTeReIrPt, and 6-element SnTeReOsIrPt single crystals (Supplementary Figs. 46–48).

With the activation of all 5 or 6 different $[MCl_6]^{2-}$ octahedral molecules in a particular crystal system upon photoexcitation at a suitable wavelength, we would expect to observe radiative and non-radiative relaxation processes from all 5 or 6 different isolated octahedra likely through confined excitons.[19,20] This behavior leads to the aforementioned hypothesis that the

emission spectrum of each HES composition is a superposition of spectral features from each $[MCl_6]^{2-}$ octahedral molecule. However, we do not observe this behavior in the emission spectrum for the high entropy 5-element ZrSnTeHfPt single crystals. The 5-element ZrSnTeHfPt HES composition exhibits gold emission centered at 580 nm (Figs. 6a and 6b) with Commission Internationale de l'Eclairage (CIE) chromaticity coordinates of (0.49, 0.49) under 250 nm excitation (Fig. 6c). It is well established in Cs_2MCl_6 literature that 1-element Cs_2SnCl_6 single crystals do not emit,[33] that 1-element Cs_2ZrCl_6 and Cs_2HfCl_6 single crystals exhibit strong blue emission,[34,35] that 1-element Cs_2TeCl_6 single crystals exhibit yellow emission,[18] and that Cs_2PtCl_6 single crystals exhibit red emission.[36] Therefore, this gold emission (Fig. 6d) results from the superposition of the confined-exciton yellow emission from $[TeCl_6]^{2-}$ octahedral molecules and the confined-exciton red emission from $[PtCl_6]^{2-}$ octahedral molecules. The blue-shift in peak wavelength positions of yellow- and red-emission spectral features in the 5-element ZrSnTeHfPt single crystals as compared to the 1-element Cs_2TeCl_6 and Cs_2PtCl_6 constituent crystals (Supplementary Fig. 49) may be brought about by (1) changes in the type of excitons formed (from self-trapped excitons in the 1-element Cs_2MCl_6 single crystals[18,36,37] to likely confined excitons in the HES single crystals) due to the inability to form a common free exciton band edge (a prerequisite for self-trapping) in a unit cell containing 5 disordered, isolated $[MCl_6]^{2-}$ octahedra, (2) changes in local strain in the unit cell from 5 different disordered metal sites with different M-Cl bond lengths, and/or (3) changes in the excited-state potential energy surface as a result of the various M-Cl bond lengths and various M-Cl molecular orbital characters in the unit cell. The complete absence of excitonic blue emission from the $[ZrCl_6]^{2-}$ and $[HfCl_6]^{2-}$ octahedral molecules in the emission spectrum of this HES composition is potentially indicative of local heterogeneity in the excited-state potential energy surface (due to the disordered nature of the unit cell) affecting the oscillator strength of the parity-allowed ground-state to excited-state transition in the $[ZrCl_6]^{2-}$ and $[HfCl_6]^{2-}$ octahedral molecules, coupled with (1) local heterogeneity in the excited-state potential energy surface affecting the efficiency of radiative decay in the $[ZrCl_6]^{2-}$ and $[HfCl_6]^{2-}$ octahedral molecules, and/or (2) energy transfer behavior from the $[ZrCl_6]^{2-}$ and $[HfCl_6]^{2-}$ octahedral molecules to the other octahedral centers in these crystals. Energy transfer between the 5 different octahedral centers in this solid-state framework is entirely feasible[33,38] given that the length scale of separation between octahedra in this unit cell

(between 3.88825 Å and 5.49878 Å) is well within the length scales of Dexter and Förster resonance energy transfer (FRET) mechanisms (below 10 Å for Dexter and below 10 nm for FRET)[39,40]. Indeed, energy transfer behavior is demonstrated in the high entropy 5-element ZrSnTeHfPt single crystals through photoluminescence excitation (PLE) spectroscopy (Supplementary Section 3, Supplementary Figs. 50–53), whereby the excited state origin of the gold emission band under 250 nm excitation is from the $[ZrCl_6]^{2-}$ and/or $[HfCl_6]^{2-}$ octahedral molecules, thereby confirming the process of energy transfer from the less strongly confined $[ZrCl_6]^{2-}$ and/or $[HfCl_6]^{2-}$ exciton states to the more strongly confined $[TeCl_6]^{2-}$ and/or $[PtCl_6]^{2-}$ exciton states in this HES composition. The energy transfer process is also demonstrated in the high entropy 6-element ZrSnTeHfRePt single crystals via PLE, thereby implying that energy transfer behavior is likely present in all HES systems (Supplementary Section 4, Supplementary Figs. 54–57).

In summary, we have achieved the room-temperature and low-temperature solution syntheses of two families of high entropy metal-halide perovskite semiconductor single crystals based on the cubic Cs_2MCl_6 vacancy-ordered double perovskite structure from multielement octahedral inks. The stabilization of the various $[MCl_6]^{2-}$ isolated octahedra within solution and their ability to be well-mixed in solution appears crucial to the formation of these HES single crystals under such low energy input. The achievement of any high entropy material, especially in a single crystal form, at room-temperature or at low-temperature (80°C) is unprecedented and is a key requirement for the successful incorporation of future HES materials into electronic device architectures. The establishment of a single crystalline high entropy halide perovskite semiconductor system allows for intrinsic material property studies on the influence of the various isolated $[MCl_6]^{2-}$ octahedra on the absorption behavior, electronic structure, energy transfer phenomena, and emission properties for potential optoelectronic applications. The rational design of these metal-halide perovskite HES single crystals via mild solution synthesis techniques has the potential to be generally applied to other HES systems, particularly those with relatively low cohesive energies, for the discovery of novel high entropy magnetic or thermoelectric materials.

Main references

1. Liu, D. *et al.* Exceptional fracture toughness of CrCoNi-based medium- and high-entropy alloys at 20 kelvin. *Science* **378**, 978–983 (2022).
2. Jin, K. *et al.* Tailoring the physical properties of Ni-based single-phase equiatomic alloys by modifying the chemical complexity. *Sci. Rep.* **6**, 20159 (2016).
3. Zhang, R.-Z., Gucci, F., Zhu, H., Chen, K. & Reece, M. J. Data-Driven Design of Ecofriendly Thermoelectric High-Entropy Sulfides. *Inorg. Chem.* **57**, 13027–13033 (2018).
4. Stolze, K., Tao, J., von Rohr, F. O., Kong, T. & Cava, R. J. Sc–Zr–Nb–Rh–Pd and Sc–Zr–Nb–Ta–Rh–Pd High-Entropy Alloy Superconductors on a CsCl-Type Lattice. *Chem. Mater.* **30**, 906–914 (2018).
5. Nguyen, T. X., Liao, Y., Lin, C., Su, Y. & Ting, J. Advanced High Entropy Perovskite Oxide Electrocatalyst for Oxygen Evolution Reaction. *Adv. Funct. Mater.* **31**, 2101632 (2021).
6. Roychowdhury, S., Ghosh, T., Arora, R., Waghmare, U. V. & Biswas, K. Stabilizing n-Type Cubic GeSe by Entropy-Driven Alloying of $AgBiSe_2$: Ultralow Thermal Conductivity and Promising Thermoelectric Performance. *Angew. Chemie* **130**, 15387–15391 (2018).
7. Deng, Z. *et al.* Semiconducting High-Entropy Chalcogenide Alloys with Ambi-ionic Entropy Stabilization and Ambipolar Doping. *Chem. Mater.* **32**, 6070–6077 (2020).
8. Luo, Y. *et al.* High Thermoelectric Performance in the New Cubic Semiconductor AgSnSbSe3 by High-Entropy Engineering. *J. Am. Chem. Soc.* **142**, 15187–15198 (2020).
9. Wu, Z., Bei, H., Pharr, G. M. & George, E. P. Temperature dependence of the mechanical properties of equiatomic solid solution alloys with face-centered cubic crystal structures. *Acta Mater.* **81**, 428–441 (2014).
10. Rost, C. M., Rak, Z., Brenner, D. W. & Maria, J. Local structure of the $Mg_xNi_xCo_xCu_xZn_xO$ (x =0.2) entropy-stabilized oxide: An EXAFS study. *J. Am. Ceram. Soc.* **100**, 2732–2738 (2017).
11. Jiang, S. *et al.* A new class of high-entropy perovskite oxides. *Scr. Mater.* **142**, 116–120 (2018).

12. Jiang, B. *et al.* High-entropy-stabilized chalcogenides with high thermoelectric performance. *Science* **371**, 830–834 (2021).
13. Rombach, F. M., Haque, S. A. & Macdonald, T. J. Lessons learned from spiro-OMeTAD and PTAA in perovskite solar cells. *Energy Environ. Sci.* **14**, 5161–5190 (2021).
14. Gao, M. *et al.* The making of a reconfigurable semiconductor with a soft ionic lattice. *Matter* **4**, 3874–3896 (2021).
15. Lai, M. *et al.* Intrinsic anion diffusivity in lead halide perovskites is facilitated by a soft lattice. *Proc. Natl. Acad. Sci.* **115**, 11929–11934 (2018).
16. Protesescu, L. *et al.* Nanocrystals of Cesium Lead Halide Perovskites ($CsPbX_3$, X = Cl, Br, and I): Novel Optoelectronic Materials Showing Bright Emission with Wide Color Gamut. *Nano Lett.* **15**, 3692–3696 (2015).
17. Folgueras, M. C. *et al.* Ligand-Free Processable Perovskite Semiconductor Ink. *Nano Lett.* **21**, 8856–8862 (2021).
18. Folgueras, M. C. *et al.* Lattice Dynamics and Optoelectronic Properties of Vacancy-Ordered Double Perovskite Cs_2TeX_6 ($X = Cl^-, Br^-, I^-$) Single Crystals. *J. Phys. Chem. C* **125**, 25126–25139 (2021).
19. Blancon, J.-C. *et al.* Scaling law for excitons in 2D perovskite quantum wells. *Nat. Commun.* **9**, 2254 (2018).
20. Barfüßer, A. *et al.* Confined Excitons in Spherical-Like Halide Perovskite Quantum Dots. *Nano Lett.* **22**, 8810–8817 (2022).
21. Baimuratov, A. S. & Högele, A. Valley-selective energy transfer between quantum dots in atomically thin semiconductors. *Sci. Rep.* **10**, 16971 (2020).
22. Kovalev, D. *et al.* Resonant Electronic Energy Transfer from Excitons Confined in Silicon Nanocrystals to Oxygen Molecules. *Phys. Rev. Lett.* **89**, 137401 (2002).
23. Yeh, J.-W., Chen, Y.-L., Lin, S.-J. & Chen, S.-K. High-Entropy Alloys – A New Era of Exploitation. *Mater. Sci. Forum* **560**, 1–9 (2007).
24. Zhang, R. *et al.* Short-range order and its impact on the CrCoNi medium-entropy alloy. *Nature* **581**, 283–287 (2020).
25. Gali, A. & George, E. P. Tensile properties of high- and medium-entropy alloys. *Intermetallics* **39**, 74–78 (2013).

26. Anand Sekhar, R., Samal, S., Nayan, N. & Bakshi, S. R. Microstructure and mechanical properties of Ti-Al-Ni-Co-Fe based high entropy alloys prepared by powder metallurgy route. *J. Alloys Compd.* **787**, 123–132 (2019).
27. Solari, S. F. *et al.* Stabilization of Lead-Reduced Metal Halide Perovskite Nanocrystals by High-Entropy Alloying. *J. Am. Chem. Soc.* **144**, 5864–5870 (2022).
28. Karim, M. M. S. *et al.* Anion Distribution, Structural Distortion, and Symmetry-Driven Optical Band Gap Bowing in Mixed Halide Cs_2SnX_6 Vacancy Ordered Double Perovskites. *Chem. Mater.* **31**, 9430–9444 (2019).
29. Hendrickson, W. A., Smith, J. L. & Sheriff, S. Direct phase determination based on anomalous scattering. in *Methods in Enzymology* vol. 115 41–55 (1985).
30. Evans, G. & Pettifer, R. F. CHOOCH: a program for deriving anomalous-scattering factors from X-ray fluorescence spectra. *J. Appl. Crystallogr.* **34**, 82–86 (2001).
31. Luo, H., Li, Z. & Raabe, D. Hydrogen enhances strength and ductility of an equiatomic high-entropy alloy. *Sci. Rep.* **7**, 9892 (2017).
32. Kovalenko, M. V., Protesescu, L. & Bodnarchuk, M. I. Properties and potential optoelectronic applications of lead halide perovskite nanocrystals. *Science* **358**, 745–750 (2017).
33. Zhong, Y. *et al.* Multi-Dopant Engineering in Perovskite Cs_2SnCl_6: White Light Emitter and Spatially Luminescent Heterostructure. *Inorg. Chem.* **60**, 17357–17363 (2021).
34. Abfalterer, A. *et al.* Colloidal Synthesis and Optical Properties of Perovskite-Inspired Cesium Zirconium Halide Nanocrystals. *ACS Mater. Lett.* **2**, 1644–1652 (2020).
35. Saeki, K., Fujimoto, Y., Koshimizu, M., Yanagida, T. & Asai, K. Comparative study of scintillation properties of Cs_2HfCl_6 and Cs_2ZrCl_6. *Appl. Phys. Express* **9**, 042602 (2016).
36. Wu, R., Liu, Y., Hu, S., Fu, P. & Xiao, Z. Red-Emitting Perovskite Variant Cs_2PtCl_6 Phosphor: Material Design, Luminous Mechanism, and Application in High-Color-Rendering White Light-Emitting Diodes. *Adv. Opt. Mater.* **10**, 2201081 (2022).
37. McCall, K. M., Morad, V., Benin, B. M. & Kovalenko, M. V. Efficient Lone-Pair-Driven Luminescence: Structure–Property Relationships in Emissive $5s^2$ Metal Halides. *ACS Mater. Lett.* **2**, 1218–1232 (2020).
38. Chang, T. *et al.* Efficient Energy Transfer in Te^{4+}-Doped Cs_2ZrCl_6 Vacancy-Ordered

Perovskites and Ultrahigh Moisture Stability via A-Site Rb-Alloying Strategy. *J. Phys. Chem. Lett.* **12**, 1829–1837 (2021).

39. MacManus, J. P., Hogue, C. W., Marsden, B. J., Sikorska, M. & Szabo, A. G. Terbium luminescence in synthetic peptide loops from calcium-binding proteins with different energy donors. *J. Biol. Chem.* **265**, 10358–10366 (1990).

40. Yun, C. S. *et al.* Nanometal Surface Energy Transfer in Optical Rulers, Breaking the FRET Barrier. *J. Am. Chem. Soc.* **127**, 3115–3119 (2005).

Figures

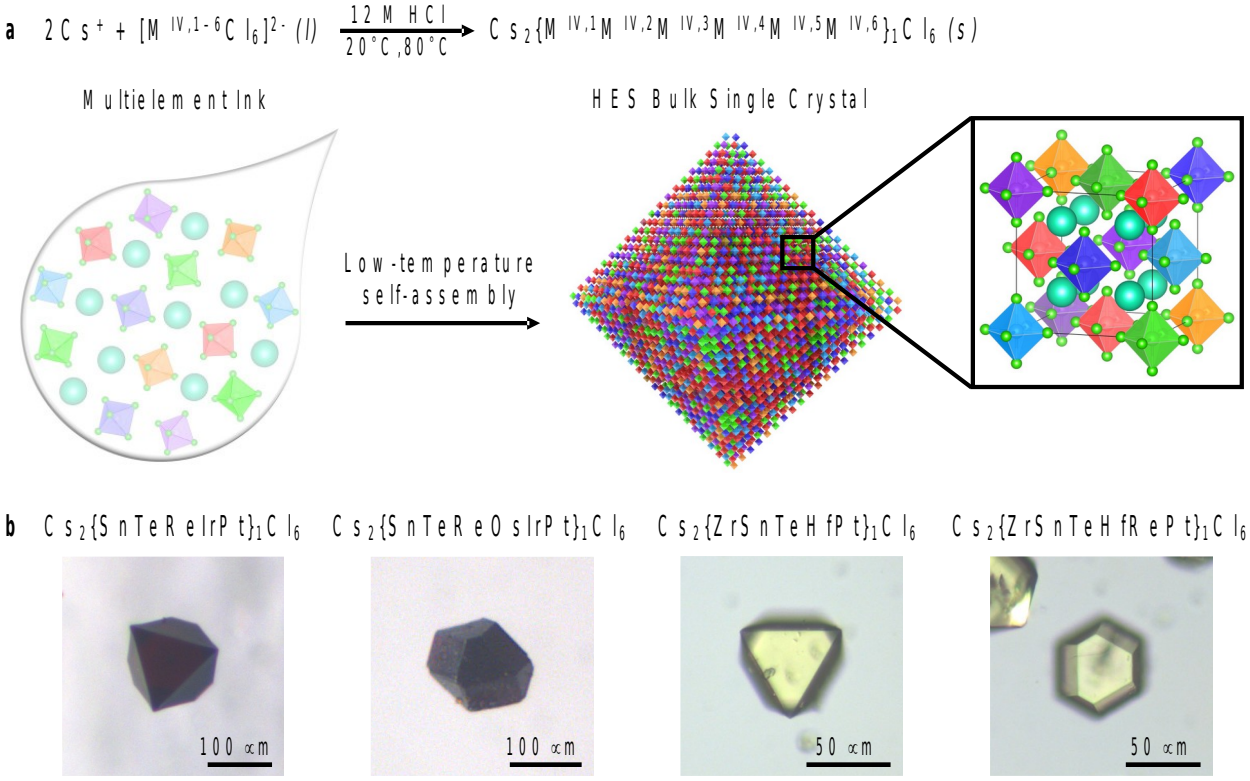

Fig. 1 | Synthetic design of high entropy 5-element and 6-element Cs_2MX_6 single crystals. a, Schematic representation of the room-temperature-driven and low-temperature-driven self-assembly processes in solution from multielement inks to high entropy semiconductor (HES) perovskite single crystals. Utilizing 12 M HCl as the solvent for the multielement inks is a specific design choice, as the excess chloride environment promotes the formation of the 6-coordinated $[MCl_6]^{2-}$ octahedral molecules in solution[41,42]. **b**, Optical microscope images of the

high entropy 5-element $Cs_2\{SnTeReIrPt\}_1Cl_6$, 6-element $Cs_2\{SnTeReOsIrPt\}_1Cl_6$, 5-element $Cs_2\{ZrSnTeHfPt\}_1Cl_6$, and 6-element $Cs_2\{ZrSnTeHfRePt\}_1Cl_6$ single crystals.

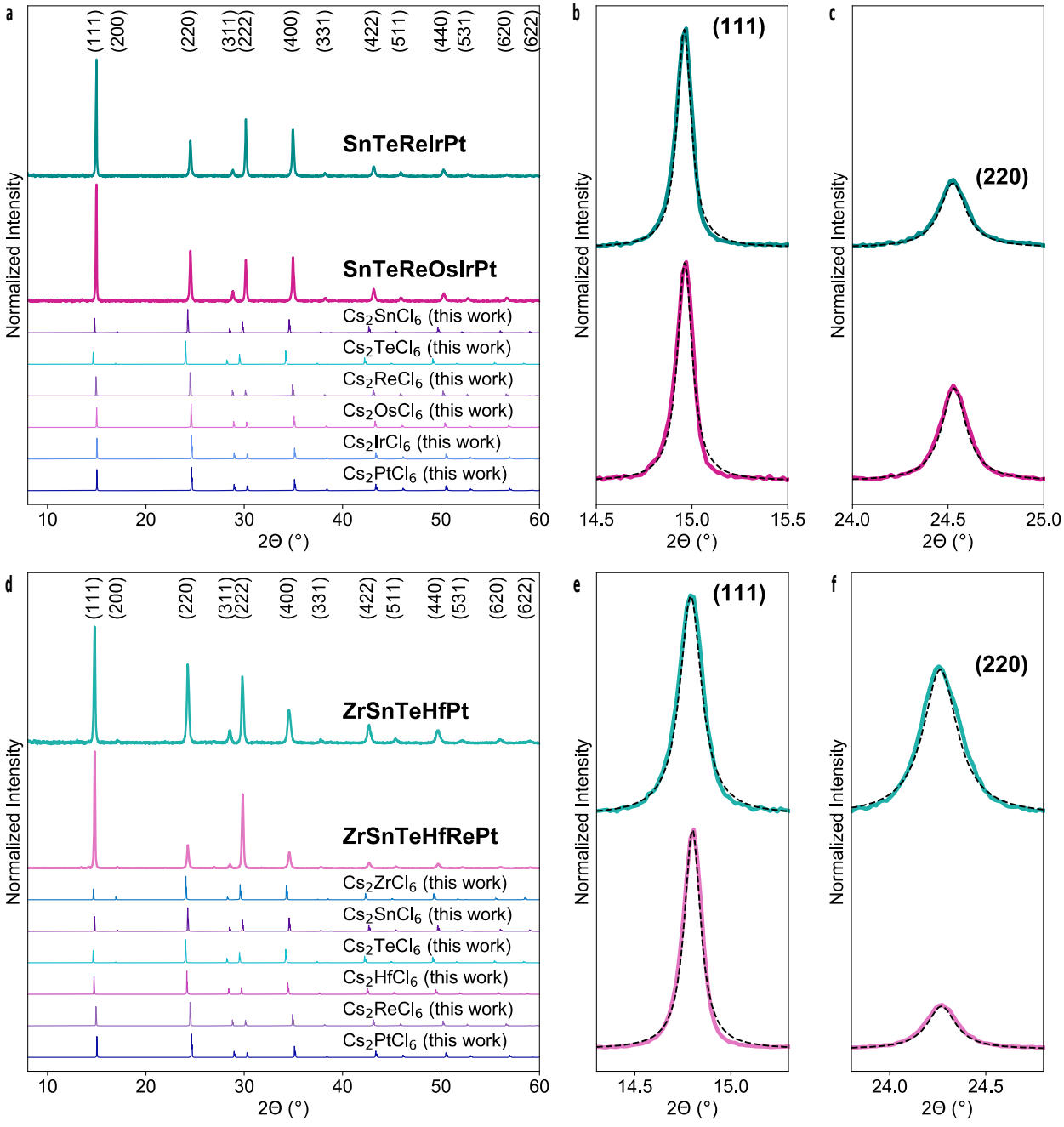

Fig. 2 | Phase identification of the 5-element and 6-element high entropy perovskite single crystals. Powder X-ray diffraction (PXRD) patterns of **a**, the 5-element $Cs_2\{SnTeReIrPt\}_1Cl_6$ and 6-element $Cs_2\{SnTeReOsIrPt\}_1Cl_6$ single crystals and **d**, the 5-element $Cs_2\{ZrSnTeHfPt\}_1Cl_6$ and 6-element $Cs_2\{ZrSnTeHfRePt\}_1Cl_6$ single crystals, all showing that

the 4 high entropy compositions adopt a single-phase face-centered cubic (FCC) crystal structure. **b**, **e**, Fine scan over the FCC (111) reflection reveals no peak splitting and a good fit to a single Lorentzian curve (black dashed line). **c**, **f**, Fine scan over the FCC (220) reflection reveals no peak splitting and a good fit to a single Lorentzian curve (black dashed line).

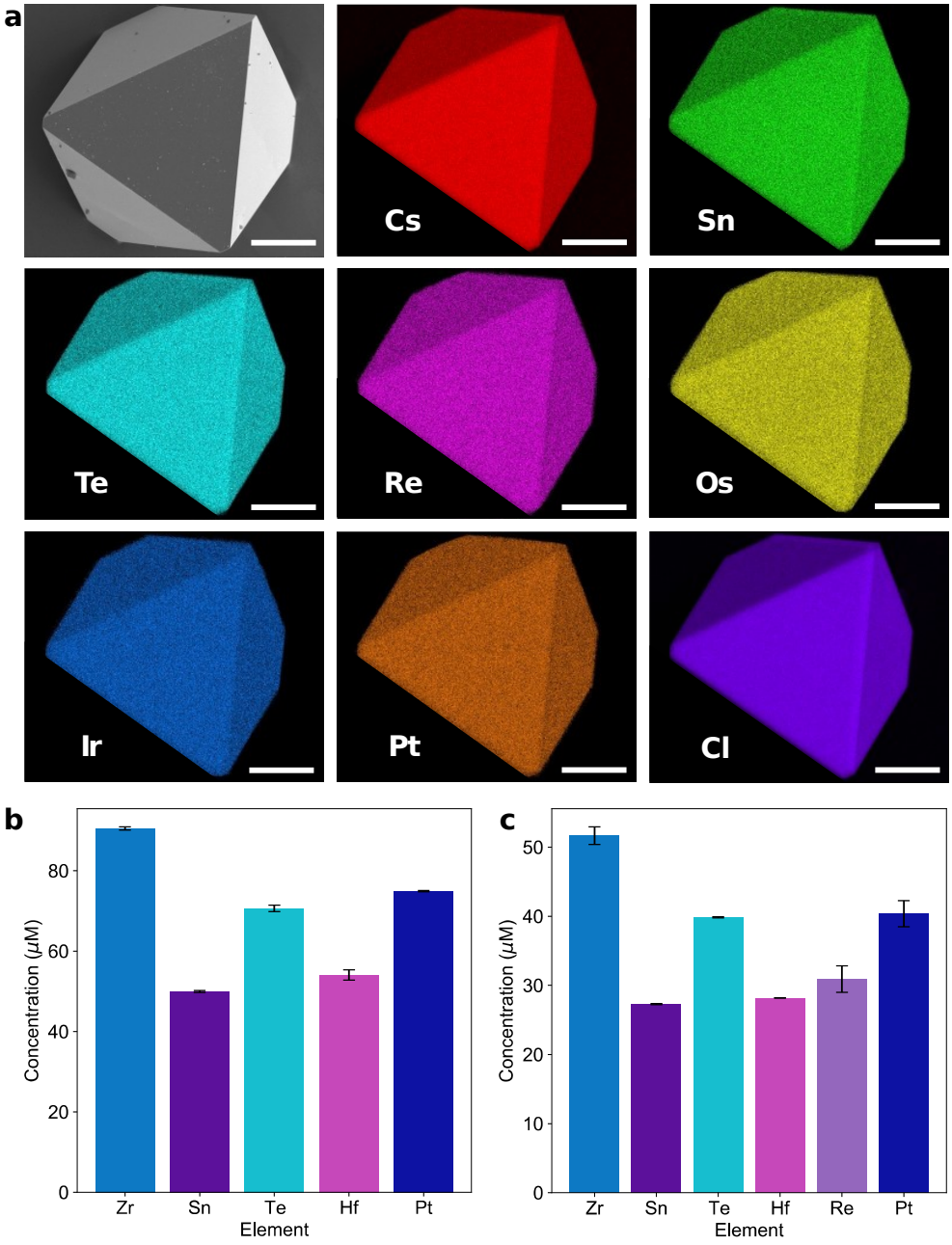

Fig. 3 | Elemental analysis of the high entropy perovskite single crystals to confirm incorporation of 5 or 6 elements on the M-site. a, Energy-dispersive X-ray spectroscopy

(EDX) mapping of a 6-element SnTeReOsIrPt single crystal confirms the incorporation and homogeneous distribution of all 6 M-site elements across a single domain. The quantitative molar concentrations (μM) of each M-site element as determined by inductively coupled plasma atomic emission spectroscopy (ICP-AES) for **b**, the 5-element ZrSnTeHfPt single crystals and **c**, the 6-element ZrSnTeHfRePt single crystals.

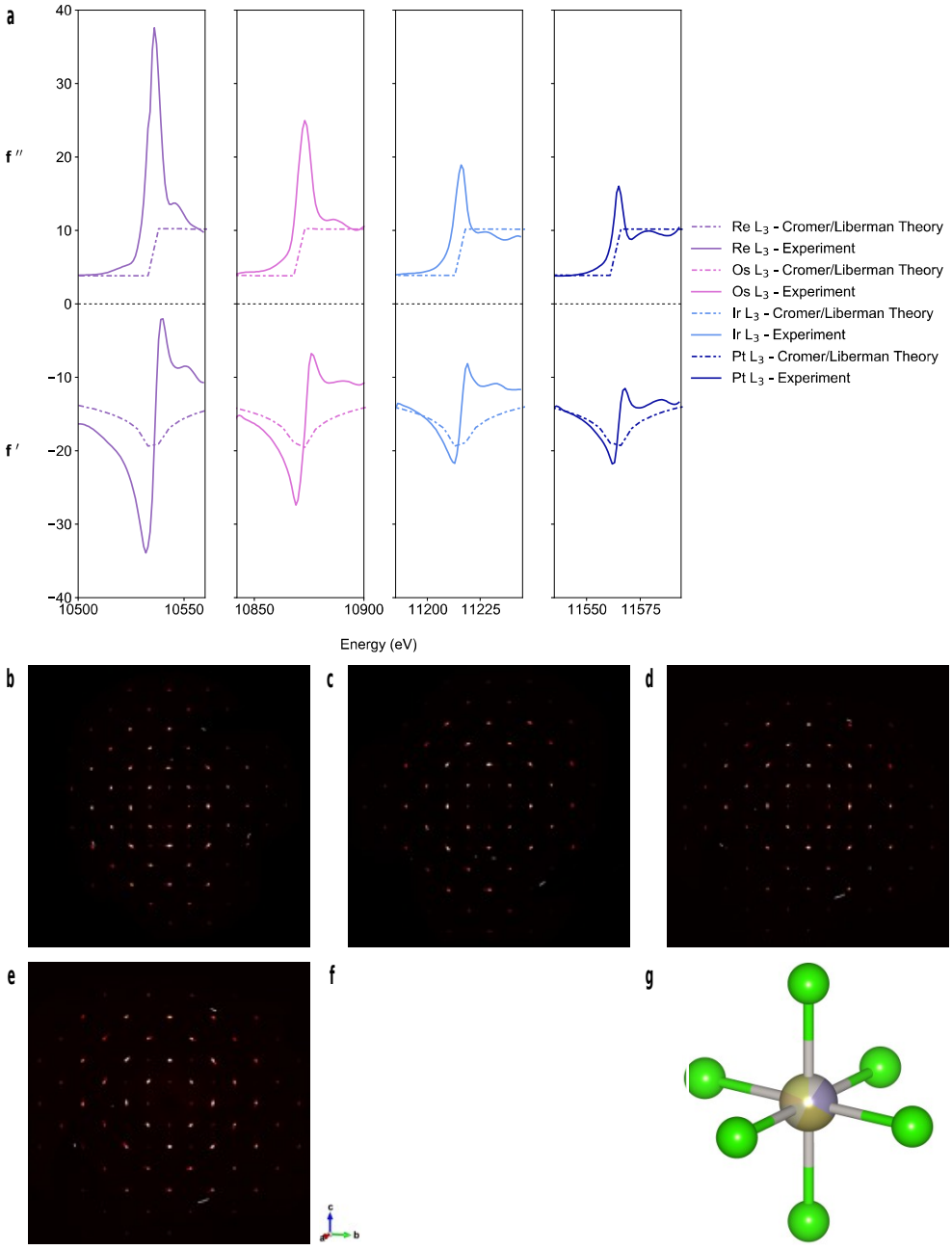

Fig. 4 | Highly resolved structure determination of the absolute configuration of M-site metal centers in the high entropy perovskite single crystals. a, Comparison of the theoretically- and experimentally-derived real and imaginary components of the anomalous scattering factor near the Re L_3-edge, Os L_3-edge, Ir L_3-edge, and Pt L_3-edge in a 6-element SnTeReOsIrPt single crystal. Edge positions of the real and imaginary components align quite well between theory and experiment. Slight deviations in edge position and more significant deviations in edge and post-edge shape between experiment and theory arise from the experimental fluorescence spectra containing information about the oxidation state and coordination environment of the element being probed. **b–e**, *0kl* plane diffraction pattern precession images at **b**, the Re L_3-edge (E = 10533 eV), **c**, the Os L_3-edge (E = 10869 eV), **d**, the Ir L_3-edge (E = 11212 eV), and **e**, the Pt L_3-edge (E = 11562 eV) of a 6-element SnTeReOsIrPt single crystal. **f**, **g**, A more highly resolved structural determination of a 6-element SnTeReOsIrPt single crystal confirms that the crystal perfectly assumes a face-centered cubic (FCC) lattice with the 6 different $[SnCl_6]^{2-}$, $[TeCl_6]^{2-}$, $[ReCl_6]^{2-}$, $[OsCl_6]^{2-}$, $[IrCl_6]^{2-}$, and $[PtCl_6]^{2-}$ octahedra all incorporated and completely disordered in the unit cell and across the single crystal. M-site element color code, starting at purple and moving clockwise: purple is Sn, dark gold is Te, dark gray is Re, orange is Os, yellow is Ir, and light gray is Pt.

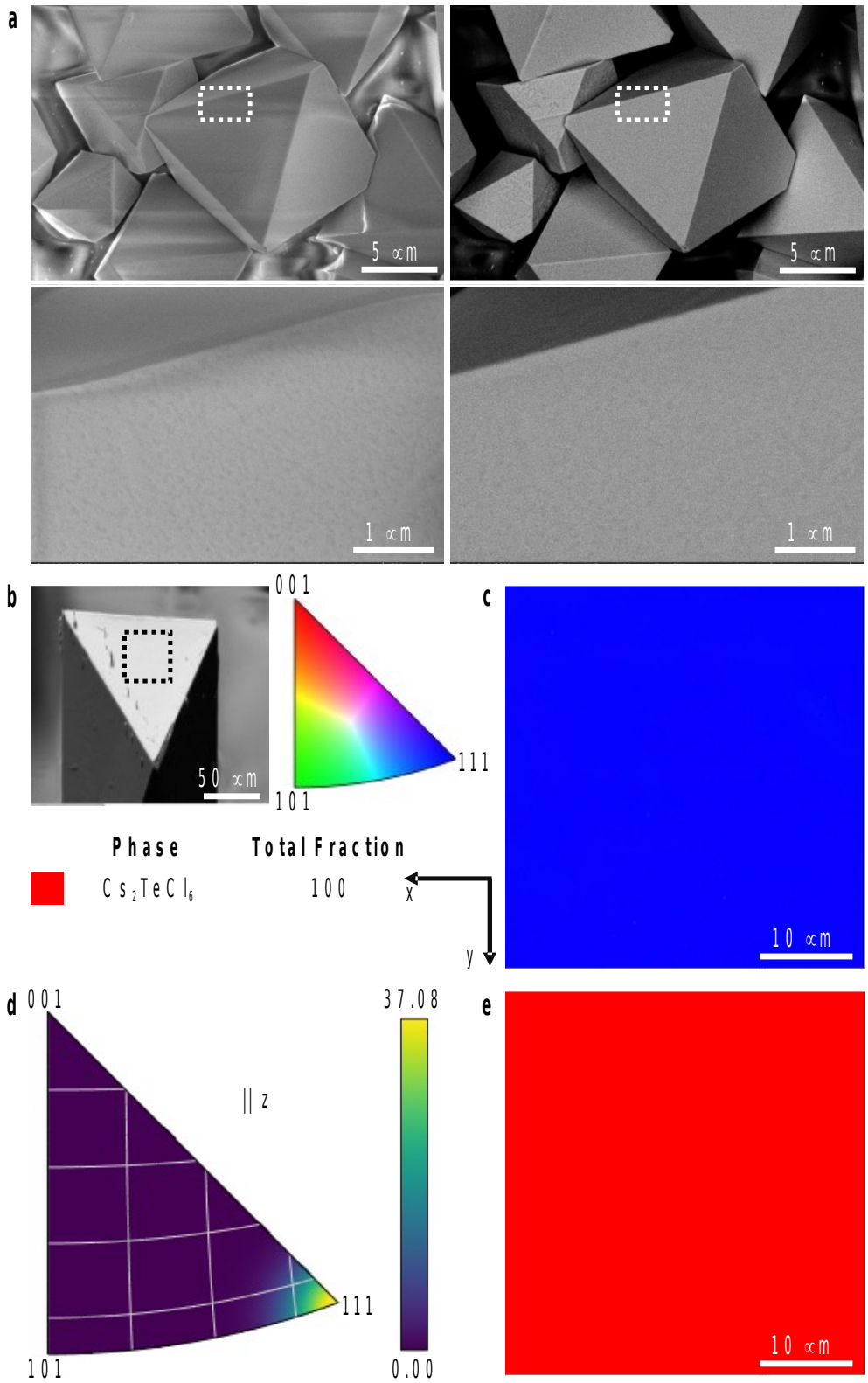

Fig. 5 | Confirmation of the disordered nature of the 5 or 6 different $[MCl_6]^{2-}$ octahedral complexes throughout the single-phase high entropy perovskite systems with no

microstructural grain formation. a, Scanning electron microscope (SEM) images of a 6-element ZrSnTeHfRePt single crystal using (left) secondary electrons and (right) backscattered electrons. (Top) A view of the entire single crystal. (Bottom) A zoomed-in view of the single crystal in the region indicated in the top images with the white-dashed box. **b**, The 6-element SnTeReOsIrPt single crystal analyzed via electron backscattered diffraction (EBSD), with the specific measurement region indicated by the black-dashed box on the exposed crystal facet. **c**, The inverse pole figure (IPF) of the measured region on the crystal facet, revealing that the entire region (by only being colored blue) possesses a single orientation of the FCC (111) close-packed plane (as evidenced by the IPF color key in **b**). **d**, The IPF contour confirms that the measured region on the crystal facet possesses an orientation corresponding to the FCC (111) close-packed plane, which is consistent with the triangular geometry of the exposed facet. **e**, The EBSD phase map of the measured region on the crystal facet, revealing that the entire region possesses a single lattice parameter and thus corresponds to a single crystal phase. The Cs_2TeCl_6 phase (colored red, as shown in the phase color key in **b**) is arbitrarily assigned for purposes of confirming single-phase formation as opposed to micrograin formation of potentially different phases.

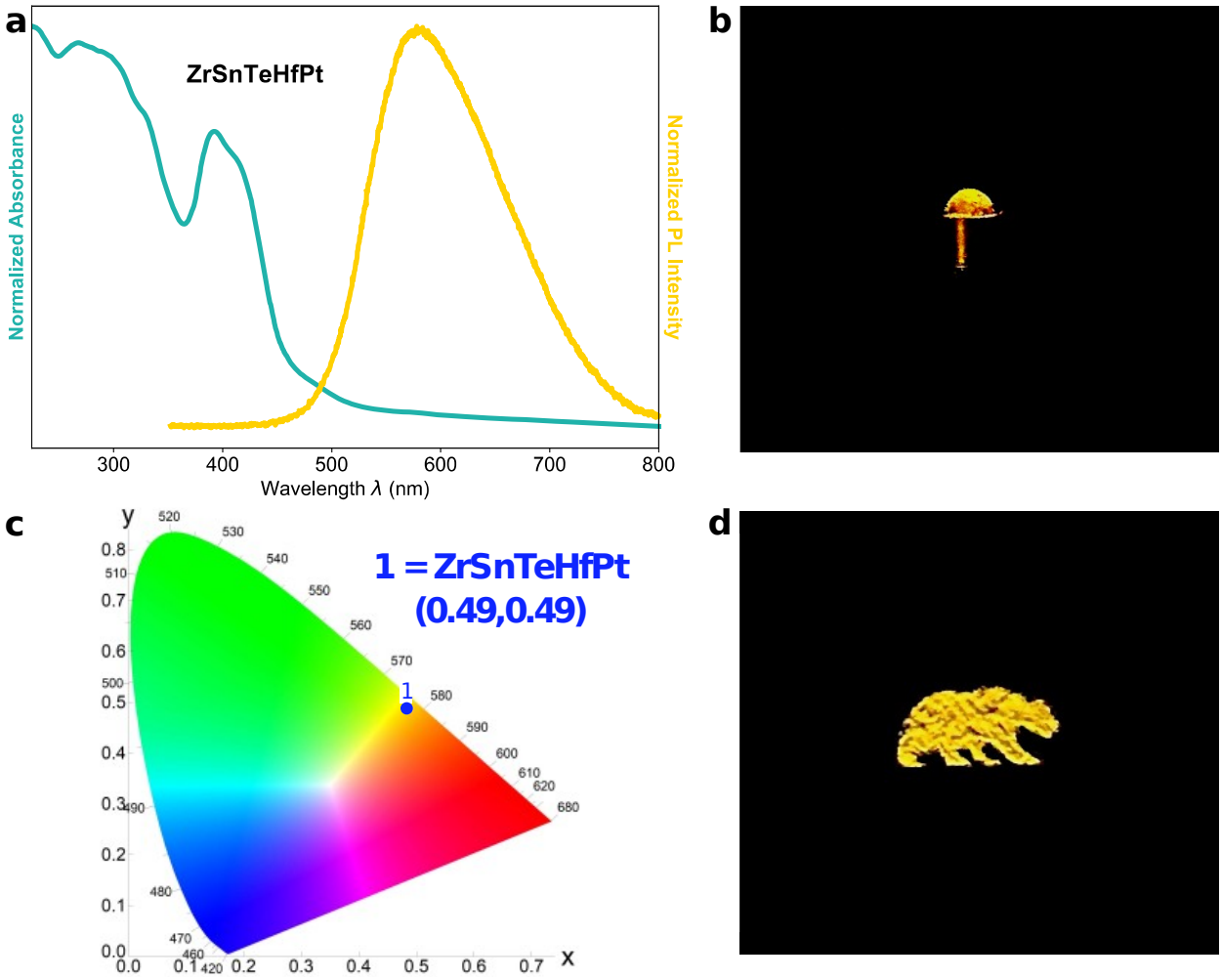

Fig. 6 | Optoelectronic behavior of the high entropy perovskite single crystals. a, UV-visible absorption spectrum and photoluminescence (PL) spectrum of the 5-element ZrSnTeHfPt single crystals. **b**, A photograph of the bright gold emission from the 5-element ZrSnTeHfPt single crystals with excitation from a 250 nm light-emitting diode (LED). **c**, Chromaticity of the emission from the 5-element ZrSnTeHfPt single crystals (λ_{ex} = 250 nm) on a Commission Internationale de l'Eclairage (CIE) diagram, located at coordinates (0.49, 0.49). **d**, PL image of the "Cal Golden Bear" emission from the 5-element ZrSnTeHfPt single crystals under UV lamp excitation (λ_{ex} = 254 nm). The crystals are formed into the bear mascot shape using a shadow mask.

Methods

Materials. CsCl (≥99.999%, Sigma Aldrich), $ZrCl_4$ (99.99%, Sigma Aldrich), $SnCl_4$ (99.995%, Sigma Aldrich), $TeCl_4$ (99.9%, Alfa Aesar), $HfCl_4$ (99.9%, Sigma Aldrich), K_2ReCl_6 (99.99%, Sigma Aldrich), K_2OsCl_6 (Os 38.7% min, Fisher Scientific), K_2IrCl_6 (99.99%, Sigma Aldrich), $PtCl_4$ (≥99.99%, Sigma Aldrich), and 12 M hydrochloric acid (HCl, 37%, Sigma Aldrich) were used as received without further purification or modification.

General procedure for Cs_2ZrCl_6, Cs_2SnCl_6, Cs_2TeCl_6, Cs_2HfCl_6, and Cs_2PtCl_6 powders. The stoichiometric amount of $ZrCl_4$, $SnCl_4$, $TeCl_4$, $HfCl_4$, or $PtCl_4$ precursor was dissolved in a vial containing 12 M HCl at room-temperature (20°C), and the stoichiometric amount of CsCl precursor was dissolved in a separate vial containing 12 M HCl at 20°C. The CsCl stock solution was then rapidly added to the $ZrCl_4$, $SnCl_4$, $TeCl_4$, $HfCl_4$, or $PtCl_4$ stock solution at 20°C. Cs_2ZrCl_6, Cs_2SnCl_6, Cs_2TeCl_6, Cs_2HfCl_6, or Cs_2PtCl_6 powders, respectively, immediately precipitated out of solution at ~100% yield. The excess solution was removed, and the powders were washed with ethanol, blown with N_2 gas to dry, and stored under vacuum in a benchtop desiccator.

General cation exchange procedure for Cs_2ReCl_6, Cs_2OsCl_6, and Cs_2IrCl_6 powders. The stoichiometric amount of K_2ReCl_6, K_2OsCl_6, or K_2IrCl_6 powder was dissolved in an uncapped vial containing 12 M HCl at 100°C and 1000 rpm spin speed (using a magnetic stir bar). The stoichiometric amount of CsCl precursor was dissolved in a separate vial containing 12 M HCl at 20°C. The K_2ReCl_6, K_2OsCl_6, or K_2IrCl_6 stock solutions were removed from the hot plate, the stir bar was removed from the stock solutions, and the CsCl stock solution was then rapidly added to each stock solution. Cs_2ReCl_6, Cs_2OsCl_6, or Cs_2IrCl_6 powders, respectively, immediately precipitated out of solution at ~100% yield. The excess solution was removed, and the powders were washed with ethanol, blown with N_2 gas to dry, and stored under vacuum in a benchtop desiccator.

General single crystal procedure for the $Cs_2\{SnTeReOsIrPt\}_1Cl_6$ HES family. Single crystals in the $Cs_2\{SnTeReOsIrPt\}_1Cl_6$ HES family are produced from an appropriate multielement ink via a low-temperature (80°C) reprecipitation synthesis (Fig. 1a). The stoichiometric amount of

Cs_2SnCl_6, Cs_2TeCl_6, Cs_2ReCl_6, Cs_2OsCl_6, Cs_2IrCl_6, and Cs_2PtCl_6 powders were dissolved in an uncapped vial containing 5 mL of 12 M HCl at 100°C and 1000 rpm spin speed (using a magnetic stir bar). Utilizing 12 M HCl as the solvent for these multielement inks is a specific design choice, as the excess chloride environment promotes the formation of the 6-coordinated $[MCl_6]^{2-}$ octahedral molecules in solution[41,42]. Once all powders were dissolved, the stir bar was removed from the solution, the vial was returned to the hot plate, and the hot plate was turned down to 80°C. The vial remained uncapped and at 80°C during the entire synthesis duration. The synthesis was deemed complete when sufficient single crystals were at the bottom of the vial and when there was only a small amount of acid solution left. The excess solution was removed, and the single crystals were washed with ethanol, blown with N_2 gas to dry, and stored in a vacuum desiccator. 100% of the precipitates were single crystals of the desired single-phase composition. No other structures or products were formed during any of the syntheses or washing processes.

General single crystal procedure for the $Cs_2\{ZrSnTeHfRePt\}_1Cl_6$ HES family. Single crystals in the $Cs_2\{ZrSnTeHfRePt\}_1Cl_6$ HES family are produced from an appropriate multielement ink via a room-temperature (20°C) reprecipitation synthesis (Fig. 1a). A very dilute, stoichiometric amount of Cs_2ZrCl_6, Cs_2SnCl_6, Cs_2TeCl_6, Cs_2HfCl_6, Cs_2ReCl_6, and Cs_2PtCl_6 powders were dissolved in a capped vial containing 20 mL of 12 M HCl at room temperature (20°C) and 1000 rpm spin speed (using a magnetic stir bar). Utilizing 12 M HCl as the solvent for these multielement inks is a specific design choice, as the excess chloride environment promotes the formation of the 6-coordinated $[MCl_6]^{2-}$ octahedral molecules in solution[41,42]. Once all powders were dissolved, the solution was left to sit in the capped vial at 20°C until the synthesis was complete. The synthesis was deemed complete when sufficient single crystals were at the bottom of the vial. The excess solution was removed, and the single crystals were washed with ethanol, blown with N_2 gas to dry, and stored in a vacuum desiccator. 100% of the precipitates were single crystals of the desired single-phase composition. No other structures or products were formed during any of the syntheses or washing processes.

Formation mechanism of the high entropy 5-element $Cs_2\{SnTeReIrPt\}_1Cl_6$, 6-element $Cs_2\{SnTeReOsIrPt\}_1Cl_6$, 5-element $Cs_2\{ZrSnTeHfPt\}_1Cl_6$, and 6-element

$Cs_2\{ZrSnTeHfRePt\}_1Cl_6$ single crystals. The apparent thermodynamic stability and spontaneous mixing of the 5- and 6-element HES single crystals is most likely due to their lower Gibbs free energy of formation (ΔG_{mix}) as compared to all other single crystals discussed (which includes the 1-, 2-, 3-, and 4-element single crystals) and even as compared to phase-segregated or amorphous systems. The Gibbs free energy of formation depends on the entropy of mixing ($\Delta G_{mix} = \Delta H_{mix} - T\Delta S_{mix}$), and the entropy of mixing is partially determined by the configurational entropy of the system. Since configurational entropy relies on the number of microstates or constituent components/particles in a system, packing more elements into the multielement inks and into the resulting crystal structures of the 5- and 6-element HES compositions corresponds to a larger configurational entropy contribution to the entropy of mixing. This in turn results in a larger entropy of mixing term and a more negative (i.e., lower) Gibbs free energy of formation for the HES compositions as compared to other products. As a point of reference, the Gibbs free energy of formation, the entropy of mixing, and the enthalpy of mixing have been reported for the $Cs_2Sn_{1-x}Te_xCl_6$ (x = 0-1) system[43]. For the $Cs_2Sn_3Te_3Cl_6$ composition (which is equivalent to low entropy 2-element SnTe single crystals reported here), the Gibbs free energy of formation is calculated to be approximately -24 meV/formula unit. Therefore, the Gibbs free energy of formation will continue to decrease below this value of -24 meV/formula unit with an increasing number of elements (3, 4, 5, or 6) on the M-site in the $Cs_2\{SnTeReOsIrPt\}_1Cl_6$ HES family. Similar behavior is expected for the $Cs_2\{ZrSnTeHfRePt\}_1Cl_6$ HES family.

Optical microscope imaging. Optical microscopy was performed to visualize the single crystals using a Nikon SMZ-2T Trinocular stereo microscope with a 6.3X objective in reflection mode (utilizing an external light source) for the $Cs_2\{SnTeReOsIrPt\}_1Cl_6$ HES family and using a Nikon Eclipse E600 polarizing microscope with a 20X objective in transmission mode for the $Cs_2\{ZrSnTeHfRePt\}_1Cl_6$ HES family.

Powder X-ray diffraction. Powder X-ray diffraction (PXRD) data were collected using a Bruker D8 laboratory diffractometer with a Cu Kα ($\lambda_{K\alpha1}$ = 1.5406 Å, $\lambda_{K\alpha2}$ = 1.54439 Å) radiation source in ambient condition. Data was collected from $2\theta = 8° - 60°$ with a step size of

0.0181027°/s. The single crystals were ground into powders on glass for measurement. Data were analyzed using single Lorentzian functions in the Multipeak Fitting 2 procedure in the IGOR Pro software.

Single-crystal X-ray diffraction. The single-crystal X-ray diffraction (SCXRD) data were collected at the Small Molecule X-ray Crystallography Facility (CheXray) in the College of Chemistry at UC Berkeley. SCXRD were measured with a Rigaku XtaLAB P200 instrument equipped with a MicroMax-007 HF microfocus rotating anode and a Pilatus 200K hybrid pixel array detector using either monochromated Mo Kα radiation (λ = 0.71073 Å) or monochromated Cu Kα radiation (λ = 1.54184 Å). All crystal datasets were collected at room temperature (293 K). CrysAlisPro[44] was used for data collection and data processing, including a multi-scan absorption correction applied using the SCALE3 ABSPACK scaling algorithm within CrysAlisPro. Using Olex2[45], the structures were solved with the SHELXT[46] structure solution program using Intrinsic Phasing and refined with the SHELXL[47] refinement package using Least Squares minimization. The metal site was separated into a disorder of all potentially incorporated metals (i.e., Zr, Sn, Te, Hf, Re, Ir, Os, Pt) by applying the EXYZ constraint. The occupancy of each incorporated metal was assigned to reflect the molar fraction of each element obtained from the results of inductively coupled plasma atomic emission spectroscopy (ICP-AES) experiments.

Scanning electron microscopy, energy-dispersive X-ray spectroscopy, and electron backscatter diffraction. A field-emission scanning electron microscope (Thermo Fisher Scientific Scios 2 FIB/SEM) allowed for visualization of single crystal morphologies via the secondary electron (SE) detector and for visualization of potential atomic number contrast across an entire crystal domain via the backscattered electron (BSE) detector. The energy-dispersive X-ray spectroscopy (EDX) detector was used to determine elemental ratios, and the electron backscatter diffraction (EBSD) detector was used to determine a single grain/single orientation in an entire crystal domain. The single crystals were placed and pressed onto double-sided conducting copper tape supported by an aluminum SEM pin stub. The samples utilized for standard SE imaging and for EDX elemental mapping were sputter-coated with gold before

measurement, while the samples utilized for BSE imaging and for EBSD grain and phase mapping were not sputter-coated.

Inductively coupled plasma atomic emission spectroscopy. Inductively coupled plasma atomic emission spectroscopy (ICP-AES) measurements were collected at the UC Berkeley College of Chemistry Microanalytical Facility using a Perkin Elmer ICP Optima 7000 DV Spectrometer.

Ultra-low-frequency Raman spectroscopy. The Raman spectra were measured by a confocal Raman microscope system (Horiba LabRAM HR Evolution) at the Stanford Nano Shared Facilities (SNSF). The single crystals were dispersed on glass for measurement. Either a continuous-wave (cw) 632.8 nm laser or a cw 785 nm laser was focused onto a crystal facet at a constant power density set by neutral density filters. The Raman signal from the sample was collected using a microscope objective in a back-scattering geometry (100X, NA 0.6). For the 632.8 nm laser, ultra-low-frequency (ULF) Raman spectra were measured with an Andor Newton DU970P BVF EMCCD detector equipped with a diffraction grating of 1800 gr/mm and an ULF filter package (10 cm^{-1}) to remove the Rayleigh scattering line from the signal. For the 785 nm laser, low-frequency (LF) Raman spectra were measured with the same detector equipped with a diffraction grating of 600 gr/mm and a notch filter (~35-40 cm^{-1}) to remove the Rayleigh scattering line from the signal. Data were analyzed using the Multipeak Fitting 2 procedure in the IGOR Pro software, implementing Lorentzian oscillators.

Multiwavelength anomalous diffraction. Multiwavelength anomalous diffraction (MAD) determines the crystal structure of a single crystal from diffraction data collected at wavelengths corresponding to the absorption edges of elements contained within that single crystal, particularly heavy metal elements[29]. MAD experiments were conducted at the Advanced Light Source (ALS) Small-Molecule Crystallography beamline 12.2.1 at Lawrence Berkeley National Laboratory (LBNL). Diffraction data were collected with a Bruker D85 3-circle diffractometer and a PHOTON II CPAD detector running shutterless, both of which were coupled to a channel-cut Si(111) monochromator allowing for tunability of the incident X-ray energy in the range of

6–25 keV. A reference Si(111) measurement was collected at 17.012 keV. Anomalous diffraction experiments were conducted at the Re L_3-edge (10.5353 keV), Os L_3-edge (10.8709 keV), Ir L_3-edge (11.2152 keV), and Pt L_3-edge (11.5637 keV) for the $Cs_2\{SnTeReOsIrPt\}_1Cl_6$ single crystal and at the Zr K-edge (17.9976 keV), Hf L_3-edge (9.5607 keV), Re L_3-edge (10.5353 keV), and Pt L_3-edge (11.5637 keV) for the $Cs_2\{ZrSnTeHfRePt\}_1Cl_6$ single crystal, and X-ray fluorescence spectra were collected from those same absorption resonances using an Amptek XR-100SSD X-ray detector. All crystal datasets were collected at room temperature (298 K). Data were reduced using the SAINT program (version 8.38A)[48] and were analyzed for agreement using XPREP (part of the APEX3 software suite, version 2017.3–0)[49]. The data were corrected for absorption with SADABS[50], selecting a 0.02 scale factor for the restraint EDS and "Strong Absorber" for the absorption type. Using the Olex2 software package[45], the structures were solved with SHELXT[46] and refined using a full-matrix least squares on F^2 with SHELXL[47]. In the *CHOOCH* software, the raw X-ray fluorescence spectra were background subtracted, smoothed using spline fits, and normalized to obtain the imaginary component of the anomalous scattering factor f'' near each L_3 absorption edge, and the imaginary component was then used to calculate the real component of the anomalous scattering factor f' using the K–K relation[30].

Ultraviolet-visible-near infrared absorption spectroscopy. The absorption spectra of the samples were measured by an ultraviolet-visible-near infrared (UV-vis-NIR) spectrophotometer (Shimadzu UV-2600). Data was collected in absorption mode over a wavelength range of 200 nm and 900 nm with a slow scanning rate. The single crystals were ground into a powder with $BaSO_4$ powder and measured with an integrating sphere attachment.

Photoluminescence spectroscopy. Photoluminescence (PL) measurements were collected with a home-built PL microscope system. The single crystals were crushed onto UV-grade quartz for measurement. A broadband deuterium lamp (Thorlabs SLS204 Stabilized Deuterium Lamp) was filtered down to a 250 nm excitation line using a bandpass filter (250 nm/10 nm). The 250 nm excitation line was focused obliquely onto the sample with a constant power density. The PL signal from the sample was collected using a microscope objective (50X) coupled to a longpass filter (cut-on wavelength: 325 nm) to remove the excitation line from the signal. Visible

wavelength PL spectra were collected under a 5 s exposure time with a Si charge-coupled device (CCD) detector cooled to -120°C via liquid nitrogen and equipped with a diffraction grating of 150 gr/mm.

Photoluminescence imaging. The gold emission light-emitting diode (LED) photograph was taken by combining the 5-element $Cs_2\{ZrSnTeHfPt\}_1Cl_6$ single crystals with a 250 nm LED. The 5-element $Cs_2\{ZrSnTeHfPt\}_1Cl_6$ single crystals were crushed on glass and transferred onto the LED by moving the LED across the crushed single crystals. The "Cal Golden Bear" emission photoluminescence (PL) image was taken by exciting the 5-element $Cs_2\{ZrSnTeHfPt\}_1Cl_6$ single crystals (which had been shaped into the Cal bear mascot) with a UV lamp (λ_{ex} = 254 nm). The bear mascot shape was achieved by generated a shadow mask of that shape, placing the shadow mask on a non-emissive substrate, weighing out the 5-element $Cs_2\{ZrSnTeHfPt\}_1Cl_6$ single crystals onto the non-emission substrate through the shadow mask, and very gently removing the shadow mask.

Photoluminescence excitation spectroscopy. Photoluminescence excitation (PLE) measurements were collected in the integrating sphere attachment of an Edinburgh FS5 spectrofluorometer. A layer of single crystals was placed in the polytetrafluoroethylene (PTFE) sample holder for measurement. Monochromatic light from a 150 W continuous-wave ozone-free Xenon (Xe) arc lamp created a wide range of excitation wavelengths that were focused onto the sample. The spectra were collected at a 1 s dwell time with a UV-enhanced Si photodiode array equipped with a diffraction grating of 1200 gr/mm.

Computational methods for molecular orbital wavefunctions and orbital energies of isolated octahedra. For each $[MCl_6]^{2-}$ ($M = Zr^{4+}$, Sn^{4+}, Te^{4+}, Hf^{4+}, Re^{4+}, Os^{4+}, Ir^{4+}, Pt^{4+}) octahedral composition, density functional theory (DFT) molecular orbital wavefunction and orbital energy calculations were performed for isolated octahedra in a vacuum using the Gaussian 16W/GaussView 6.0 software package[51]. Ground-state geometry optimization was completed for the $[ZrCl_6]^{2-}$, $[SnCl_6]^{2-}$, $[TeCl_6]^{2-}$, $[HfCl_6]^{2-}$, and $[PtCl_6]^{2-}$ octahedra such that calculations were performed at the ground-state optimized Zr–Cl bond length of 2.450 Å (expected bond length of

2.4671(10) Å from this work's Cs_2ZrCl_6 structure determination), the ground-state optimized Sn–Cl bond length of 2.423 Å (expected bond length of 2.4308(10) Å from this work's Cs_2SnCl_6 structure determination), the ground-state optimized Te–Cl bond length of 2.536 Å (expected bond length of 2.5387(9) Å from this work's Cs_2TeCl_6 structure determination), the ground-state optimized Hf–Cl bond length of 2.437 Å (expected bond length of 2.437(3) Å from this work's Cs_2HfCl_6 structure determination), and the ground-state optimized Pt–Cl bond length of 2.340 Å (expected bond length of 2.335(4) Å from this work's Cs_2PtCl_6 structure determination). Ground-state geometry optimization was not completed for the $[ReCl_6]^{2-}$, $[OsCl_6]^{2-}$, and $[IrCl_6]^{2-}$ octahedra such that calculations were performed at a Re–Cl bond length of 2.740 Å larger than the ground-state optimized bond length of 2.361 Å (expected bond length of 2.3667(17) Å from this work's Cs_2ReCl_6 structure determination), a Os–Cl bond length of 2.724 Å larger than the ground-state optimized bond length of 2.345 Å (expected bond length of 2.3450(9) Å from this work's Cs_2OsCl_6 structure determination), and a Ir–Cl bond length of 2.710 Å larger than the ground-state optimized bond length of 2.331 Å (expected bond length of 2.331(2) Å from this work's Cs_2IrCl_6 structure determination). The use of the larger bond lengths for these $[ReCl_6]^{2-}$, $[OsCl_6]^{2-}$, and $[IrCl_6]^{2-}$ octahedra is in accordance with the ligand-field-independence of the d–d electronic transition between the highest occupied molecular orbital (HOMO) t_{2g} and the lowest unoccupied molecular orbital (LUMO) e_g. As a result, the longer bond lengths for the $[ReCl_6]^{2-}$, $[OsCl_6]^{2-}$, and $[IrCl_6]^{2-}$ octahedra allow the calculations to better capture the d–d HOMO-LUMO transitions of a Re^{4+}, Os^{4+}, or Ir^{4+} center in the presence of an octahedral ligand field[52–54]. An unrestricted open-shell form of the HSE06 hybrid functional[55] was used in combination with a SDD basis set incorporating Stuttgart-Dresden effective-core potentials (ECPs)[56,57]. All isolated molecules were left in a negatively charged state (i.e., 2-) with a resultant ground-state multiplicity of: 1 for $[ZrCl_6]^{2-}$, $[SnCl_6]^{2-}$, $[TeCl_6]^{2-}$, $[HfCl_6]^{2-}$, and $[PtCl_6]^{2-}$; 2 for $[IrCl_6]^{2-}$; 3 for $[OsCl_6]^{2-}$; and 4 for $[ReCl_6]^{2-}$.

Enhanced stability of the high entropy 5-element $Cs_2\{SnTeReIrPt\}_1Cl_6$, 6-element $Cs_2\{SnTeReOsIrPt\}_1Cl_6$, 5-element $Cs_2\{ZrSnTeHfPt\}_1Cl_6$, and 6-element $Cs_2\{ZrSnTeHfRePt\}_1Cl_6$ single crystals. The 5- and 6-element HES single crystals have enhanced stability comparable to the 1-element Cs_2MX_6 (M = Te^{4+}, Sn^{4+}, Ti^{4+}, Pt^{4+}, Pd^{4+}, etc.; X =

Cl^-, Br^-, I^-) systems over the more traditional $CsMX_3$ ($M = Pb^{2+}$, Sn^{2+}, Ge^{2+}; $X = Cl^-$, Br^-, I^-) systems[58–60]. Specifically, the 5- and 6-element HES single crystals maintain the enhanced air, water, UV, and electron beam stability of some 1-element Cs_2MCl_6 crystals[43,61–64]. All four HES single crystals are stable in air for at least 6 months, which is tested by simply storing all four HES compositions in ambient conditions on a benchtop. That being said, all crystals are typically stored in an inert environment such as a vacuum desiccator as a precaution. Furthermore, the 5-element $Cs_2\{ZrSnTeHfPt\}_1Cl_6$ single crystals and the 6-element $Cs_2\{ZrSnTeHfRePt\}_1Cl_6$ single crystals are emission-stable under constant UV excitation for approximately 11 hours (reference the photoluminescence excitation (PLE) mapping results in Supplementary Figs. 50 and 56). There is no evidence of photoinduced phase segregation in the photoluminescence (PL) spectra of these materials during the 11-hour period. Finally, the 5-element $Cs_2\{SnTeReIrPt\}_1Cl_6$ single crystals and the 6-element $Cs_2\{SnTeReOsIrPt\}_1Cl_6$ single crystals are stable under all electron beam conditions, but the 5-element $Cs_2\{ZrSnTeHfPt\}_1Cl_6$ single crystals and the 6-element $Cs_2\{ZrSnTeHfRePt\}_1Cl_6$ single crystals exhibit slight electron beam instability under the conditions required for electron backscatter diffraction (EBSD). EBSD requires significantly higher accelerating voltages and beam currents than any other measurement technique, so the slight electron beam instability at the EBSD operating conditions is reasonable. The 5-element $Cs_2\{ZrSnTeHfPt\}_1Cl_6$ single crystals and the 6-element $Cs_2\{ZrSnTeHfRePt\}_1Cl_6$ HES single crystals are completely stable under all other electron beam conditions, including those for standard secondary electron (SE) imaging, backscattered electron (BSE) imaging, and energy-dispersive X-ray spectroscopy (EDX).

Data availability

The data supporting the findings of this study are available within the article and its Supplementary Information, and are available from the corresponding author upon reasonable request. The crystallographic information files (CIF) have also been deposited in the Inorganic Crystal Structure Database under reference numbers CSD 2216614–2216620, 2216624, 2216626, 2216627, and 2216636–2216643. These data can be obtained free of charge via https://www.ccdc.cam.ac.uk/structures/, or by emailing data_request@ccdc.cam.ac.uk.

Methods references

41. Zeltmann, A. H., Matwiyoff, N. A. & Morgan, L. O. Nuclear magnetic resonance of oxygen-17 and chlorine-35 in aqueous hydrochloric acid solutions of cobalt(II). I. Line shifts and relative abundances of solution species. *J. Phys. Chem.* **72**, 121–127 (1968).
42. Brady, G. W., Robin, M. B. & Varimbi, J. The Structure of Ferric Chloride in Neutral and Acid Solutions. *Inorg. Chem.* **3**, 1168–1173 (1964).
43. Tan, Z. *et al.* Lead-Free Perovskite Variant Solid Solutions $Cs_2Sn_{1-x}Te_xCl_6$: Bright Luminescence and High Anti-Water Stability. *Adv. Mater.* **32**, 2002443 (2020).
44. CrysAlisPro 1.171.39.45f.
45. Dolomanov, O. V., Bourhis, L. J., Gildea, R. J., Howard, J. A. K. & Puschmann, H. OLEX2: a complete structure solution, refinement and analysis program. *J. Appl. Crystallogr.* **42**, 339–341 (2009).
46. Sheldrick, G. M. SHELXT – Integrated space-group and crystal-structure determination. *Acta Crystallogr. Sect. A* **71**, 3–8 (2015).
47. Sheldrick, G. M. Crystal structure refinement with SHELXL. *Acta Crystallogr. Sect. C* **71**, 3–8 (2015).
48. Bruker. SAINT (Version 8.38A). Bruker AXS, Inc., Madison, WI. (2012).
49. Bruker. APEX3 (Version 2017.3-0). Bruker AXS, Inc., Madison, WI. (2012).
50. Bruker. SADABS. Bruker AXS, Inc., Madison, WI. (2017).
51. Frisch, M. J. *et al.* Gaussian, Inc., Wallingford, CT, 2016.
52. Gamelin, D. R. & Güdel, H. U. Spectroscopy and Dynamics of Re^{4+} Near-IR-to-Visible Luminescence Upconversion. *Inorg. Chem.* **38**, 5154–5164 (1999).
53. Khan, S. M., Patterson, H. H. & Engstrom, H. Multiple state luminescence for the d^4 $OsCl_6^{2-}$ impurity ion in K_2PtCl_6 and Cs_2ZrCl_6 cubic crystals. *Mol. Phys.* **35**, 1623–1636 (1978).
54. Douglas, I. N. Optical Spectra of $IrCl_6^{2-}$ in Single Crystals of Cs_2ZrCl_6, Cs_2HfCl_6, and K_2SnCl_6 at Low Temperatures. *J. Chem. Phys.* **51**, 3066–3073 (1969).
55. Heyd, J., Scuseria, G. E. & Ernzerhof, M. Hybrid functionals based on a screened

Coulomb potential. *J. Chem. Phys.* **118**, 8207–8215 (2003).

56. Andrae, D., Häußermann, U., Dolg, M., Stoll, H. & Preuß, H. Energy-adjusted ab initio pseudopotentials for the second and third row transition elements. *Theor. Chim. Acta* **77**, 123–141 (1990).
57. Sousa, S. F. *et al.* Comparative analysis of the performance of commonly available density functionals in the determination of geometrical parameters for zinc complexes. *J. Comput. Chem.* **30**, 2752–2763 (2009).
58. Lin, J. *et al.* Thermochromic halide perovskite solar cells. *Nat. Mater.* **17**, 261–267 (2018).
59. Lin, Z., Folgueras, M. C., Le, H. K. D., Gao, M. & Yang, P. Laser-accelerated phase transformation in cesium lead iodide perovskite. *Matter* **5**, 1455–1465 (2022).
60. Bischak, C. G. *et al.* Tunable Polaron Distortions Control the Extent of Halide Demixing in Lead Halide Perovskites. *J. Phys. Chem. Lett.* **9**, 3998–4005 (2018).
61. Yang, S. *et al.* Novel Lead-Free Material Cs_2PtI_6 with Narrow Bandgap and Ultra-Stability for Its Photovoltaic Application. *ACS Appl. Mater. Interfaces* **12**, 44700–44709 (2020).
62. Ju, M.-G. *et al.* Earth-Abundant Nontoxic Titanium(IV)-based Vacancy-Ordered Double Perovskite Halides with Tunable 1.0 to 1.8 eV Bandgaps for Photovoltaic Applications. *ACS Energy Lett.* **3**, 297–304 (2018).
63. Sakai, N. *et al.* Solution-Processed Cesium Hexabromopalladate(IV), Cs_2PdBr_6, for Optoelectronic Applications. *J. Am. Chem. Soc.* **139**, 6030–6033 (2017).
64. Xu, Y. *et al.* Zero-Dimensional Cs_2TeI_6 Perovskite: Solution-Processed Thick Films with High X-ray Sensitivity. *ACS Photonics* **6**, 196–203 (2019).

Acknowledgements

This work was primarily supported by the U.S. Department of Energy, Office of Science, Office of Basic Energy Sciences, Materials Sciences and Engineering Division, under contract no. DE-AC02-05CH11231 within the Fundamentals of Semiconductor Nanowire Program (KCPY23). The authors thank Dr. Nicholas S. Settineri at UC Berkeley and Dr. Simon J. Teat at ALS for their assistance in SCXRD and SCXRD-MAD measurements, AJ Gubser for helpful discussions

surrounding SEM-BSE imaging and EBSD measurements, and John Grimsich for providing access to the various optical microscopes in the Earth and Planetary Sciences Petrographic Microscope Resource Center. Single-crystal X-ray diffraction studies were performed at the UC Berkeley College of Chemistry Small Molecule X-ray Crystallography Facility (CheXray) and at beamline 12.2.1 of the Advanced Light Source (ALS), a U.S. DOE Office of Science User Facility at Lawrence Berkeley National Laboratory (LBNL) under contract no. DE-AC02-05CH11231. Ultra-low-frequency Raman spectroscopy was performed at the Stanford Nano Shared Facilities (SNSF), supported by the National Science Foundation under award ECCS-2026822. M.C.F. acknowledges support from the Kavli ENSI Philomathia Graduate Student Fellowship. J.J. acknowledges fellowship support from Suzhou Industrial Park.

Author contributions

M.C.F. and P.Y. conceived the idea. M.C.F., Y.J., and P.Y. designed the research. M.C.F. and Y.J. led the study and conducted the materials synthesis, major characterization, and data analysis including PXRD, SCXRD, SEM imaging, SEM-EDX, SEM-EBSD, ICP-AES, Raman, UV-vis, PL, and theoretical calculations. Y.J. and J.J. conducted the SCXRD-MAD experiments. M.C.F. conducted the X-ray fluorescence analysis, and J.J. analyzed the SCXRD-MAD datasets. M.C.F., Y.J., and P.Y. wrote the manuscript. All authors discussed the results and revised the manuscript.

Author information

These authors contributed equally: Maria C. Folgueras, Yuxin Jiang

Competing interests

The authors declare no competing financial interests.

Funding

This work was primarily supported by the U.S. Department of Energy, Office of Science, Office of Basic Energy Sciences, Materials Sciences and Engineering Division, under contract no. DE-AC02-05CH11231 within the Fundamentals of Semiconductor Nanowire Program (KCPY23).

Corresponding author

Correspondence to Peidong Yang (p_yang@berkeley.edu)